

A Sub-Picojoule per Bit Integrated Magneto-Optic Modulator on Silicon: Modeling and Experimental Demonstration

Marijn P. G. Rombouts,* Fotini Karinou, Paolo Pintus, Duanni Huang, John E. Bowers, and Nicola Calabretta

Integrated magneto-optic (MO) modulators are an attractive but not fully explored alternative to electro-optic (EO) modulators. They are current driven, structurally simple, and could potentially achieve high efficiency in cryogenic and room temperature environments where $f\text{J bit}^{-1}$ optical interfaces are needed. In this paper, the performance and energy efficiency of a novel MO modulator at room temperature are for the first time assessed. First, a model of the micro-ring-based modulator is implemented to investigate the design parameters and their influence on the performance. Then, a fabricated device is experimentally characterized to assess its performance in terms of bit rate and energy efficiency. The model shows efficient operation at 1.2 Gbps using a 16 mA drive current, consuming only $155 f\text{J bit}^{-1}$. The experimental results show that the MO effect is suitable for modulation, achieving error-free operation above 16 mA with a power consumption of $258 f\text{J bit}^{-1}$ at a transient limited data rate of 1.2 Gbps.

1. Introduction

Increasing demands for artificial intelligence, machine learning and 5G networks are boosting the growth of datacenters while imposing tight energy requirements on cloud operators. Higher data rates and increased energy efficiency are needed to reduce both the operation expenditure and the environmental impact. In order to meet these requirements, it is apparent that innovation is required to design more efficient and faster optical interconnects.^[1] To that end, optical modulator efficiencies have to be pushed towards $f\text{J bit}^{-1}$ regimes to reduce the end-to-end link efficiency to a few pJ bit^{-1} .^[2]

Efficiencies of $f\text{J bit}^{-1}$ have been demonstrated so far in the literature by various voltage-driven, electro-optic (EO) modulators.^[3–6] Complementary to these EO modulators, early works have proposed the concept of current-driven modulators using magneto-optic (MO) effects. In such devices, the modulation is achieved via the change of the magnetic field induced by an alternating current.^[7–9] MO devices have the exclusive capability to interface with other current-driven circuits, enabling various applications where this compatibility is the key.^[7] The efficiency of MO devices could potentially be decreased by orders of magnitude by decreasing the required current. This can be achieved by making use of efficient MO materials, by exploiting the efficiency improvements of these materials at low temperatures^[7,10–12] and by co-integration with superconductive circuits.^[9] This makes such a device a compelling solution not only for future classical networking architectures, but also for solving the interconnect bottleneck in quantum computing architectures.^[13] “ $f\text{J bit}^{-1}$ ” interfaces are needed to transfer information from cryogenic environments to room temperature, a challenge which currently hinders the scalability of such architectures beyond tens of qubits.^[14,15] Various MO integrated devices have been reported over the years, for example, optical isolators,^[16–18] (plasmonic) circulators,^[19–21] and sensors.^[22] A theoretical magneto-plasmonic phase-shifter has been proposed,^[23] but practical MO modulators have not been thoroughly investigated.

In this work, we investigate the potential of MO modulators based on a micro-ring resonator (MRR) structure. The small size


M. P. G. Rombouts, N. Calabretta
Department of Electrical Engineering
Eindhoven Hendrik Casimir Institute
Eindhoven University of Technology
PO Box 513, Eindhoven 5600 MB, The Netherlands
E-mail: m.p.g.rombouts@tue.nl

F. Karinou
Microsoft Research Ltd.
21 Station Road, Cambridge CB1 2FB, UK

P. Pintus, J. E. Bowers
Department of Electrical and Computer Engineering
University of California
Santa Barbara, CA 93106, USA

P. Pintus
Department of Physics
University of Cagliari
Monserrato 09042, Italy

D. Huang
Intel Corporation
2200 Mission College Blvd, Santa Clara, CA 95054, USA

 The ORCID identification number(s) for the author(s) of this article can be found under <https://doi.org/10.1002/lpor.202200799>

© 2023 The Authors. Laser & Photonics Reviews published by Wiley-VCH GmbH. This is an open access article under the terms of the Creative Commons Attribution-NonCommercial-NoDerivs License, which permits use and distribution in any medium, provided the original work is properly cited, the use is non-commercial and no modifications or adaptations are made.

DOI: 10.1002/lpor.202200799

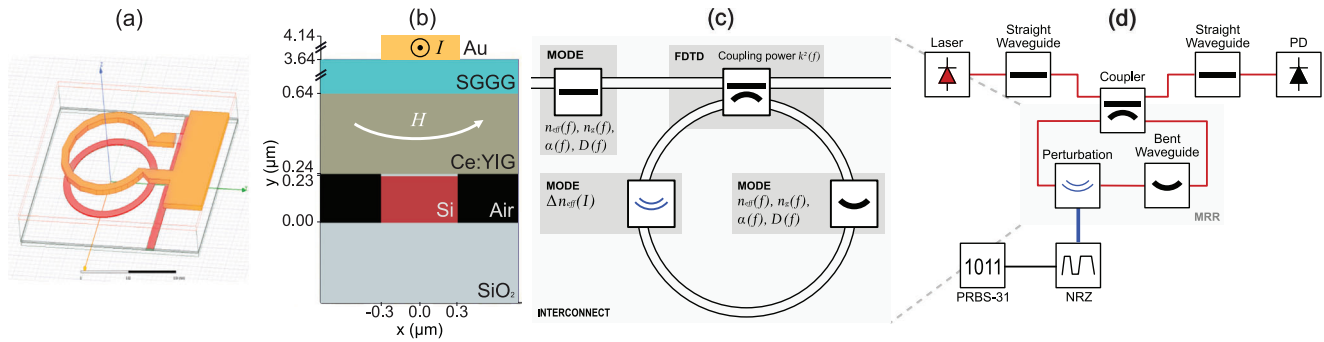


Figure 1. a) The electrical HFSS model with the waveguides in green and the coil in red. b) The current magnetic field strength relationship calculated from HFSS for various SGGG layer thicknesses. c) A detailed overview of all components in the MRR device model. d) The circuit simulation set-up in INTERCONNECT.

of MRRs improves driving speeds and relaxes the power consumption. A detailed electrical and optical simulation model is developed to infer on the performance and energy efficiency of the MO modulator. First, the electrical model is developed using the electromagnetic field solver ANSYS HFSS. The electrical properties (resistance and inductance) of the electromagnet are evaluated and the magnetic field strength is measured at the interface of the MO layer. Then, using Lumerical's MODE solver, the electrical information is used to calculate the MO effect and to determine the impact on the waveguide properties. The MO effect is combined with the MRR to assess its performance and efficiency using the optical circuit simulator Lumerical INTERCONNECT. At last, a comparable fabricated MRR based MO device is experimentally characterized in the lab to assess its transmission performance, efficiency, and the bandwidth of the MO effect. Our results show that the model is able to accurately describe the MO effect and that it delivers solid results when combined with a MRR structure. Data rates exceed 10 Gbps when an ideal MO response is assumed. The experimental characterization of the actual MO device shows error-free operation above 16 mA, achieving a power consumption of 258 fJ bit⁻¹ at a transient limited data rate of 1.2 Gbps. Higher data rates could possibly improve efficiency.

2. Magneto-Optic Modulators

When an MO material is exposed to an external magnetic field, energy levels within the matter split according to the Zeeman effect.^[24] This splitting has an impact on the optical properties of the material and causes anisotropic and gyrotropic behavior.^[25,26] The presence of the magnetic field causes electron spins, which are aligned along and opposite to the field, to have different levels of energy. One effect is a distinction in material permittivity for left- and right-handed circularly polarized light: $\epsilon_{r,LHCP}$ and $\epsilon_{r,RHCP}$, respectively. The strength of the MO effect is given by either the Verdet constant V in $^{\circ} \text{T}^{-1} \text{m}^{-1}$ or the Faraday Rotation θ_F in $^{\circ} \text{cm}^{-1}$.

Its primary optical effects can be distinguished by the orientation of the magnetic field with respect to the propagation direction of the optical field. For integrated waveguide structures the non-reciprocal phase shift (NRPS) effect^[27] is exploited which is induced as follows. When the magnetic field is perpendicular to the direction of propagation, the longitudinal propagation

constant can be changed magnetically resulting in a phase shift. When a microstrip is placed on top of the structure as shown in Figure 1b, parallel to the waveguide, the magnetic field is perpendicular and induces the NRPS effect in the MO layer. With an asymmetric waveguide structure, where the MO layer is on top of the waveguide, the NRPS effect causes a forward propagating TM polarized wave to experience a change in effective index when the rotating (or reflecting) electric field component of the propagating wave overlaps with the magnetically biased MO material. To modulate light, the polarity of the magnetic field is changed.

Various MO materials exist differing in optical transparency, MO effect strength and ease of fabrication.^[7,10–12,28–31] For the device under study in this paper, cerium substituted yttrium iron garnet (Ce:YIG) is used. It conveys a relatively low transparency of 60 dB cm⁻¹ and a strong MO effect of $-4800^{\circ} \text{cm}^{-1}$ for a saturating in-plane magnetic field strength of only 50 Oe.^[20] The latter is important to achieve a low power consumption.

Applying this material on top of optical structures such as MRRs and Mach-Zehnder interferometers (MZIs), the MO effect can be used to control the output intensity by shifting the spectrum or by means of interference^[16,17] For MRRs, the spectrum can be shifted by changing the effective index n_{eff} . In a MRR, the resonant wavelength is

$$\lambda_0 = \frac{n_{\text{eff}}(\lambda_0)L}{m}, \quad \text{with } m = 1, 2, 3, \dots \quad (1)$$

where L is the optical path length or the ring circumference and m is an integer mode number.^[32] The resonant wavelength shift (RWS) of the spectrum $\Delta\lambda$ is given by:

$$\Delta\lambda = |\lambda - \lambda_0| = \lambda \frac{\Delta n_{\text{eff}}}{n_g} \quad (2)$$

where Δn_{eff} is the effective index variation, and n_g is the group index.

3. Modulator Modeling

To evaluate the efficiency and effectiveness of the MO, various solvers of ANSYS Lumerical are used to construct a model of a MO modulator.

3.1. Modeling Non-Reciprocal Phase Shift

To describe the MO effect and to calculate the change in effective index, a permittivity tensor is used^[33]

$$\epsilon_r = \begin{pmatrix} \epsilon_{xx} & 0 & 0 \\ 0 & \epsilon_{yy} & 0 \\ 0 & 0 & \epsilon_{zz} \end{pmatrix} + K \begin{pmatrix} 0 & M_z & -M_y \\ -M_z & 0 & M_x \\ M_y & -M_x & 0 \end{pmatrix} \quad (3)$$

with ϵ_{xx} , ϵ_{yy} , and ϵ_{zz} being the diagonal material permittivities or the square of the refractive index. The MO effect is added with M being the magnetization and K a complex material parameter. When KM_x or KM_y are purely imaginary, forward, and backward modes only differ in the phase constant, which is the NRPS effect. M_z gives rise to TE-TM mode coupling, which can be neglected if the magnetization vector is in the xy -plane and the light propagates in the z -direction.

For a waveguide system using a slab Ce:YIG layer, TM wave compatible stack-up and a horizontal magnetic field perpendicular to the waveguide (x -direction) as shown in Figure 1b, the permittivity tensor becomes

$$\epsilon_r = \begin{pmatrix} \epsilon_{xx} & 0 & 0 \\ 0 & \epsilon_{yy} & j\epsilon_{yz} \\ 0 & -j\epsilon_{yz} & \epsilon_{zz} \end{pmatrix} \quad (4)$$

where the off-diagonal terms are responsible for the MO effect and are directly related to Faraday rotation constant θ_F by $\epsilon_{yz} = 2n_{\text{Ce:YIG}}\theta_F/k_0$. For Ce:YIG, the refractive index equals 2.22 and k_0 is the wavenumber defined by $2\pi/\lambda_0$.

There is no analytical description of the behavior of θ_F with respect to the magnetic field strength H for Ce:YIG. However, since Ce:YIG saturates magnetically, a good empirical approximation is^[34]

$$\theta_F(H_T) = \theta_F^0 \times \tanh \frac{H_T}{H_T^0} \quad (5)$$

where θ_F saturates to $-4800^\circ \text{ cm}^{-1}$ when $H_T > 50 \text{ Oe}$. H_T^0 is set to 24 Oe and the temperature dependence is not considered.

3.2. Simulation Methods

First, the electrical and magnetic characteristics of the device must be determined in order to quantify the strength of the MO effect. Using ANSYS HFSS, an electromagnetic field solver, the device is modeled as shown in Figure 1a. Using the frequency response of the electromagnet, its frequency dependent resistance and inductance are extracted. For various DC currents, the magnetic field strength is computed at the interface of the waveguide and MO layer.

The supported optical modes are simulated using the finite difference eigenmode solver (FDE) using Lumerical's MODE for the cross-section of a waveguide. The field within the ring is calculated by applying a conformal transformation to the result of a straight waveguide. Parameters such as β , n_{eff} , n_g and the loss are exported over a frequency range between 1500 and 1600 nm. The coupling section is simulated using a 3D finite difference time domain (FDTD) solver, where the mesh is locally refined to

ensure properly resolving fields over the gap. The coupler is assumed to be symmetric and lossless. Hence, only the coupling coefficient is evaluated.

The MO effect is modeled by activating the Ce:YIG layer in MODE by applying Equation (4) to the bent-waveguide model. The tensor is diagonalized and supplemented by a transformation matrix by calculating the eigenvalues and eigenvectors. By sweeping θ_F from $-4800^\circ \text{ cm}^{-1}$ (positive current) to $+4800^\circ \text{ cm}^{-1}$ (negative current), the change n_{eff} is calculated. θ_F is linked to the input current by Equation (5) and the HFSS model.

All data is gathered in INTERCONNECT to construct a ring resonator as shown in Figure 1c,d. The MO effect is applied as a perturbation to the ring using the difference relation between n_{eff} and I . Temperature effects and fabrication errors have not been included in the model.

4. Numerical Results

The modeled device is adapted from ref. [19], its geometry and layer stack are shown in Figure 1a,b, respectively. A 20 μm radius MRR is used with a bus waveguide to ring waveguide gap of 250 nm. The silicon-on-insulator (SOI) device is wafer bonded to the MO material, which is deposited on a lattice matched substituted gadolinium gallium garnet (SGGG) substrate. On top of the structure, a single-turn gold coil is deposited. The waveguides of 600 by 230 nm support TM polarized waves. On top of the waveguide, a 10 nm SiO_2 layer is assumed as a byproduct of the plasma activation during the wafer bonding process. The thickness of the Ce:YIG and SGGG substrate layer are 400 nm and 2 μm , respectively. The thickness of the SGGG layer has been reduced to the lowest thickness found in literature to improve magnetic coupling for maximum MO efficiency.^[20] It is noteworthy that achieving this thickness is not straightforward. Likewise, the Faraday rotation for the Ce:YIG is set to the strongest figure found, where the material is deposited in a way that is similar or equal to the reference device.^[20]

4.1. Electromagnetic Field Analysis

The thickness of the SGGG layer determines the degree of magnetic coupling, as shown in Figure 2a. For a 2 μm thick SGGG layer, the magnetic field strength is linearly related to the electromagnet current with a rate of 257 Oe A^{-1} . At 10 μm , it has decreased to 112 Oe A^{-1} . Given the simple structure of the electromagnet, a series equivalent circuit containing a resistor and inductor is assumed. Its frequency dependency is shown in Figure 2b. Below 10 GHz, the frequency characteristics of electromagnet are constant, giving a resistance of 0.68 Ω and an inductance of 77.4 pH. The coil of gold is 1.5 μm thick, 3 μm wide. The resistance increases due to the skin-effect, leading to an increase in power consumption at higher frequencies.

4.2. Ring Resonator Characteristics

The TM modal fields within the ring are shown in Figure 3a,b. The E_y component of the TM wave shows an evanescent tail into

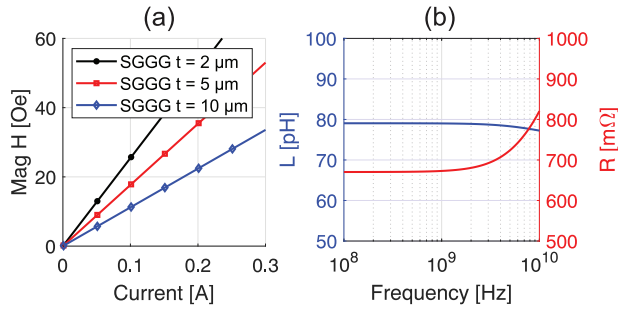


Figure 2. a) The magnetic field strength calculated from HFSS for various SGGG layer thicknesses. b) Inductance and resistance of the modeled electromagnet over various frequencies. The coil of gold is 1.5 μm thick and 3 μm wide.

the Ce:YIG layer and a strong confinement in the SiO_2 layer. The impact of this SiO_2 buffer on the propagation loss is clear when the layer is removed, as the loss increases from 29.68 to 35.62 dB cm^{-1} . The real parts of the effective index (n_{eff}) and group index (n_g) are measured to be 2.262 and 3.484, respectively. Based on results from the characterized MO device (Section 5), n_g is set to 4.5, to match the model to the characterized device.

In the coupling section, where the ring resonator meets the bus waveguide, the coupling coefficients are obtained by simulating a bus waveguide and a quarter bent waveguide with the same stack-up as for the previously simulated waveguides. Various gap widths are evaluated, for which the cross-coupling coefficients $1 - t^2$ and the round-trip loss coefficients $1 - a^2$ (black dashed lines) are calculated in Figure 3c. The round-trip loss is invariant to the gap since the result is equal for each variant. At 1550 nm and a gap width of 250 nm, 9% of the power is found to couple into the ring. The waveguide loss in dB within the ring is calculated using $-4.34 \log a^2/L$ and equals 29.86 dB cm^{-1} . Com-

binning the results into INTERCONNECT, the optical spectrum is calculated as shown in Figure 3d. Notice how the minima align with the intersections of t^2 and a^2 in Figure 3c. By controlling the gap, the critical coupling point can be shifted and the shape of the notch can be controlled. By fitting Lorentzian curves to each notch in the spectrum, the effect of the gap on the full-width half-maximum (FWHM) is demonstrated in Figure 3e. For a gap of 250 nm at 1548 nm, we observe an FSR of 4.19 nm, an FWHM of 0.120 nm, a Q-factor of 12874 and a Finesse of 34.82.

Figure 3f shows the MO effect for various combinations of design parameters. The legend can be found in Figure 3g. The design parameters stepped from the most optimal model to a model that matches the characterized device (more on this in Section 5). All parameters affecting the modulator performance and efficiency are included, these include the Faraday Rotation (θ_F), SGGG layer thickness (t), the MRR gap width (g), and n_g . The impact of an error in n_g is demonstrably large, whereas the gap width has no impact. The opposite is true for the analytically evaluated extinction ratio (ER) in Figure 3g. Here, the gap width is the main differentiator in the modulator characteristic, and the impact of the MO strength is negligible. With a 250 nm gap, the ER settles to 26 dB after tens of mA. The model using a tighter gap of 220 nm settles to 12 dB, mainly due to the overcoupled configuration which reduces the achievable ER. The efficiency of the device can be found in the steepness of the curve for low currents, where the MO strength causes negligible differences. The efficiency is affected by the increase in FWHM (or decrease in Q-factor) by using a tighter ring resonator gap.

4.3. Transmission Modeling

Next, the transmission characteristics of the modeled MO modulator are assessed in Figure 4. Figure 4a demonstrates the

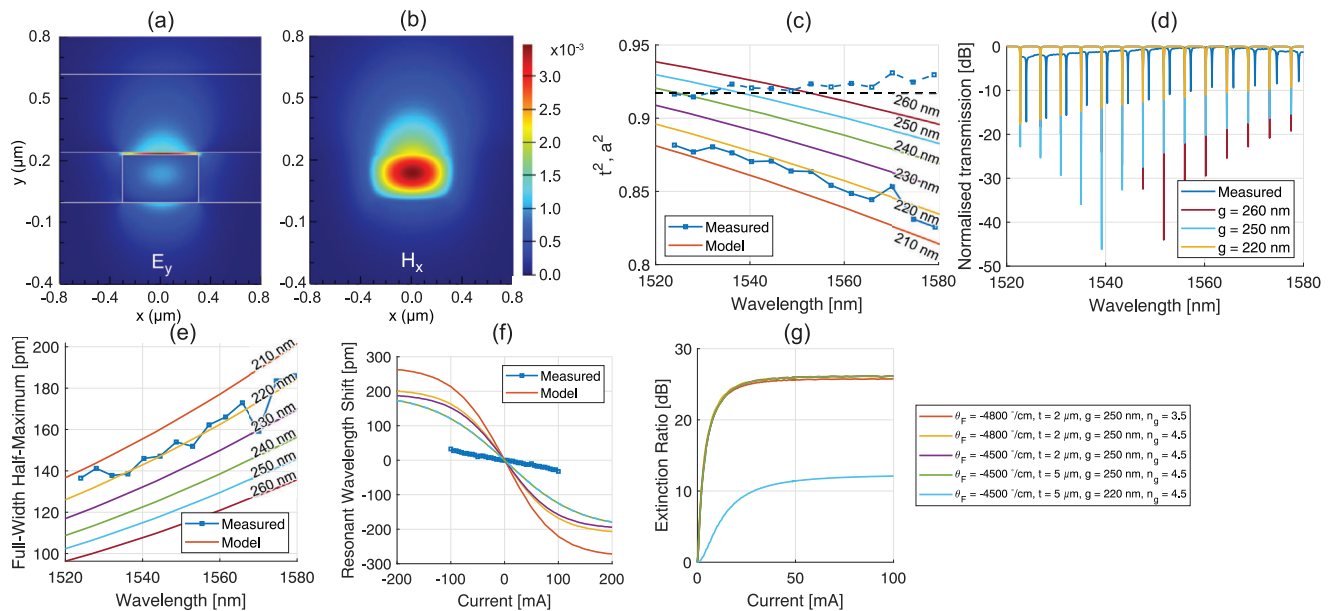


Figure 3. a) The E_y component in the waveguide cross section. b) The H_x component. c) Loss and transmission coefficients (a^2 and t^2 , respectively) for various gap widths of the MRR. d) Optical transmission spectrum for various MRR gap widths. e) FWHM for various MRR gap widths. f) RWS versus the drive current for various design parameters. The legend of (g) can be used. g) ER versus current for various design parameters.

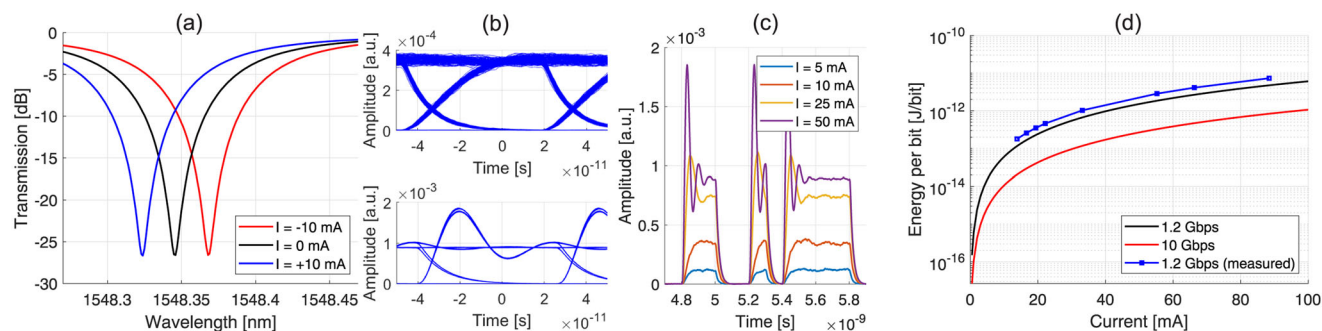


Figure 4. a) MO effect shown on the MRR spectrum with a 10 mA drive current. b) Eye-diagrams of random data with a 10 mA (top) and 50 mA (bottom) drive current at 10 Gbps. c) Waveforms of random data for various I at 10 Gbps. d) Efficiency of the modeled modulator at various bitrates, using an inductance of 77.4 pH and a resistance of 0.68 Ω , respectively. The measured line has an inductance of 200 pH and a resistance of 1 Ω .

wavelength shift for a 10 mA drive current. By applying a bipolar current (e.g., -10 mA representing a binary zero, and $+10$ mA representing a binary one), the spectral shift is maximized while a zero average current through the system is maintained. This is important to avoid steady-state losses in current drivers, which improves energy efficiency. The laser is aligned to the minimum of the notch with a negative drive current. A pseudo-random binary sequence of length $2^{31} - 1$ (PRBS-31) with non-return-to-zero (NRZ) coding is applied using various drive currents to generate the waveforms and eye-diagrams. Figure 4b shows the eye-diagram at 10 mA (top) and 50 mA (bottom) drive current at 10 Gbps. Be aware that the bitrate is limited as described in Section 4.4. The waveform and eye diagram in Figure 4b,c shows an overshoot at higher drive currents, due to the temporal wavelength shift of the trapped light within the ring during the transition. A larger RWS translates to a stronger overshoot.^[35] Due to the low current, heating effects are assumed to be minimal and the overall efficiency is expected to be high. All data are obtained using a CW laser source with a linewidth of 1 MHz and a power of 0 dBm.

To assess the efficiency of the modulator, the energy consumed per bit is calculated. Assuming a random bit sequence with an equal distribution of ones and zeros, on average a single bit is estimated to consume^[9]:

$$E_b = \frac{1}{2} LI_p^2 + I_p^2 RT_b \quad (6)$$

where L is the coil's inductance, R the equivalent resistance, I_p the peak current and T_b the bit time. The first half describes the charging and discharging of the magnetic field, halved by the random distribution of ones and zeroes. The second half describes the power dissipated per bit by resistive losses in the coil.^[9] The inductance and resistance values found in the HFSS model are used. Figure 4d shows the energy per bit E_b for various bitrates. The marked line is a comparison to the measured device, using the measured R and L as presented in Section 5. All curves saturate as the drive current increases, caused by the transfer function of the MRR. Ideally, with only 1 mA, 0.60 fJ bit⁻¹ can be achieved using 1.2 Gbps. More realistically, higher drive currents are probably needed to open the eyes with the presence of noise, as confirmed in Section 5. For example, at 16 mA, 155 fJ bit⁻¹ is achieved at 1.2 Gbps, respectively. Combined with Figure 3g, this

gives an ER of 8.7 or 24.6 dB, depending on the ring resonator gap width.

4.4. Model Limitations

Since only the necessary effects for a MO modulator have been integrated, the model will have some limitations. Among these are temperature, caused by Joule heating of the electromagnet and environmental circumstances. As the modeled currents are relatively low, Joule heating is not assumed to have impact.

Device bandwidth is essential when assessing the maximum data rate of MO modulators. To ensure the results seen in Figure 4b,c is correct, bandwidth limiting sources must be evaluated. Typically, carrier movement, electrode induced RC time constants and the optical Q -factor limit the bandwidth in case of EO based MRRs. For our MO modulator, similar sources are expected. The electromagnet induces a L/R time constant and optically the Q -factor limits the speed. Besides, the impact of the driver should be considered as this might add additional resistive losses or even add capacitive effects to the driving path. It is expected that the MO effect has a limited bandwidth, which is currently not assumed in the model.

The speed of the MO effect depends on the magnetization dynamics of the MO material, where electrons require time to adjust their spin to a changing external magnetic field. Multiple parameters describe the magnetization speed, for which the Gilbert damping α and the magnetic field strength H are the most important. When critically dampened, that is, $\alpha = 1$, the material requires $t \approx 2/\gamma\mu_0 H$ s to respond and align to the reversed magnetic field.^[36] With low damping rates ($\alpha < 1$) and low magnetic field strengths, the magnetic reversal time increases, possibly limiting switching performance. Note that the magnetization properties of the used Ce:YIG are not known and Lumerical does not have native support for this particular effect. Characterization of the device is needed to assess the actual achievable bandwidth of the device. Similar characterization results have demonstrated a modulation rate of 2 Gbps,^[9] therefore we believe the model results at 10 Gbps to be infeasible.

5. Experimental Characterization

A fabricated MO modulator is experimentally characterized to demonstrate its behavior and assess its performance. The chip has

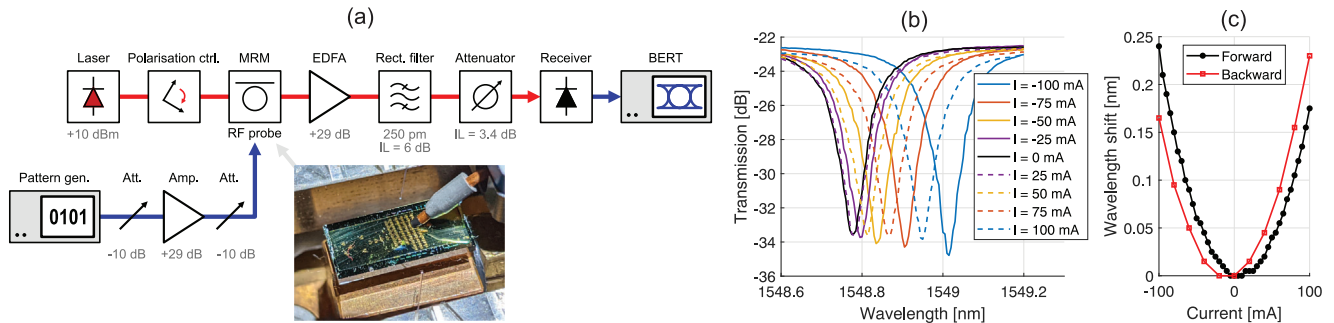


Figure 5. a) Overview of the transmission setup. Static characteristics are measured using a constant current source. The modulator is in all cases temperature controlled to 20°C, the light is coupled to the edge-couplers of the chip using lensed fibers as shown in the picture. The MO layer is just visible as the translucent layer on top. b) Spectrum of the MRR at various DC currents using a 6 dBm laser source. c) Wavelength shift with respect to the DC current for two directions of light propagation.

MRRs equal to the model in terms of geometry as described in Section 4. The MO layers differ with θ_F of $-4500^\circ \text{ cm}^{-1}$ and an SGGG layer thickness of $5 \mu\text{m}$.

The chip is vacuum mounted on a copper chuck and temperature controlled using a thermo-electric cooler (TEC) set at 20°C. The set-up is set to stabilize before performing the measurements to prevent temperature gradients from the TEC. Using lensed fibers, light is coupled in and out of the chip in TM polarization, set using a polarization controller. A schematic for transmission experiments is shown in Figure 5a. By sweeping the laser wavelength and measuring the received power, the spectrum of the ring is measured. Similar to Section 4, the ring properties have been extracted by fitting Lorentzian curves. Comparing the FWHM with the model (Figure 3e), we see that the actual device matches the results for a ring resonator with a tighter gap of 220 nm. Extracting the coupling coefficients using the methods by McKinnon et al.^[37] as shown in Figure 3c, the assumption of a smaller gap is confirmed. This difference can be explained by fabrication tolerances, as there is only a 5% difference in the waveguide width. Here, the waveguide loss is found to be similar to the model with 28.30 dB cm^{-1} .

Using a constant current source and a 40 GHz, 150 μm ground-signal probe, the current through the coil is varied with steps of 10 mA from -100 to 100 mA. By measuring the spectrum around the notch for every level of current, the spectral shift is recorded as shown in Figure 5b,c. Figure 3 shows the modeled MO shift. Besides the spectral shift, we note an insertion loss (IL) of 23 dB, which can be attributed to the large Ce:YIG surface. The measured response has a different shape, which is mainly caused by the Joule heating of the coil, causing the parabolic shape and a redshift in the MRR spectrum. The MO effect can be found in the distinction between forward and backward propagation as a result of non-reciprocity. Furthermore, Figure 3f isolates the measured MO effect by removing the redshift from the results. The MO effect is measured to be weaker than the corresponding modeled device (where the SGGG thickness equals $5 \mu\text{m}$). The discrepancy in observed MO effect is expected to be related to the mismatch seen in the group index. The latter might indicate an increase in TM mode confinement and hence dispersion. Hence, possible explanations include but are not limited to the delamination of the MO layers, existence of air bubbles between

the waveguide and MO layers, oxidation, or other structural issues caused by aging or transport.

The dominant temperature effect can be tempered by applying higher frequency signals, as the thermo-optic effect has a response time in the order of microseconds.^[38,39] A pattern generator and an RF amplifier with a high saturation power are used to supply power to the chip. Additional attenuators are added to reduce the gain and temper the reflections caused by the impedance mismatch between the RF feed and the chip. The full transmission setup is shown in Figure 5a. The modulator output has been sampled using an Agilent 83434A 10 Gbps lightwave receiver. The currents indicated in Figure 6 are determined from the peak to peak output voltage of the pattern generator and the amount of amplification and attenuation in the RF feed using

$$I_{\text{RMS}} = \sqrt{\frac{4Z_0 P_L}{(Z_0 + Z_L)(Z_0 + Z_L)^*}} \quad (7)$$

where Z_0 is the characteristic impedance of 50Ω , Z_L is the load impedance and P_L is the electrical power at the tip of the probe. The RMS current is assumed to be equal to the peak current of the data signal. For all experiments a PRBS-31 sequence is used, unless mentioned otherwise.

The waveform and eye-diagrams shown in Figure 6a show the performance at 1.2 Gbps. On both the rising and falling edges, a damped oscillation with a frequency of 1.08 GHz is visible. No deviation is observed by changing the setup or operation parameters, contrary to the transients shown in Figure 4c. As the transients can be folded over by aligning the laser wavelength to the center of the optical notch, the transient is expected to be an electrical resonance in proximity of the chip.

The bandwidth of the chip can be estimated on the rise and fall times at high bitrates. At 1.2 Gbps, the fastest edge is measured to be around 163 ps, whereas at higher bitrates, the rise time decreases to only 63 ps. Assuming a first order system response, using $\text{BW} = 0.35/\tau_{\text{rise}}$ gives a modulator bandwidth of 5.5 GHz. However, using a similar device, a 2 Gbps modulation rate has been established.^[9] Further material characterization is needed to conclusively assess the switching limitations of Ce:YIG.

Figure 6b demonstrates the BER versus the receiver input power. A commercial MZM (Integrated Optical Components

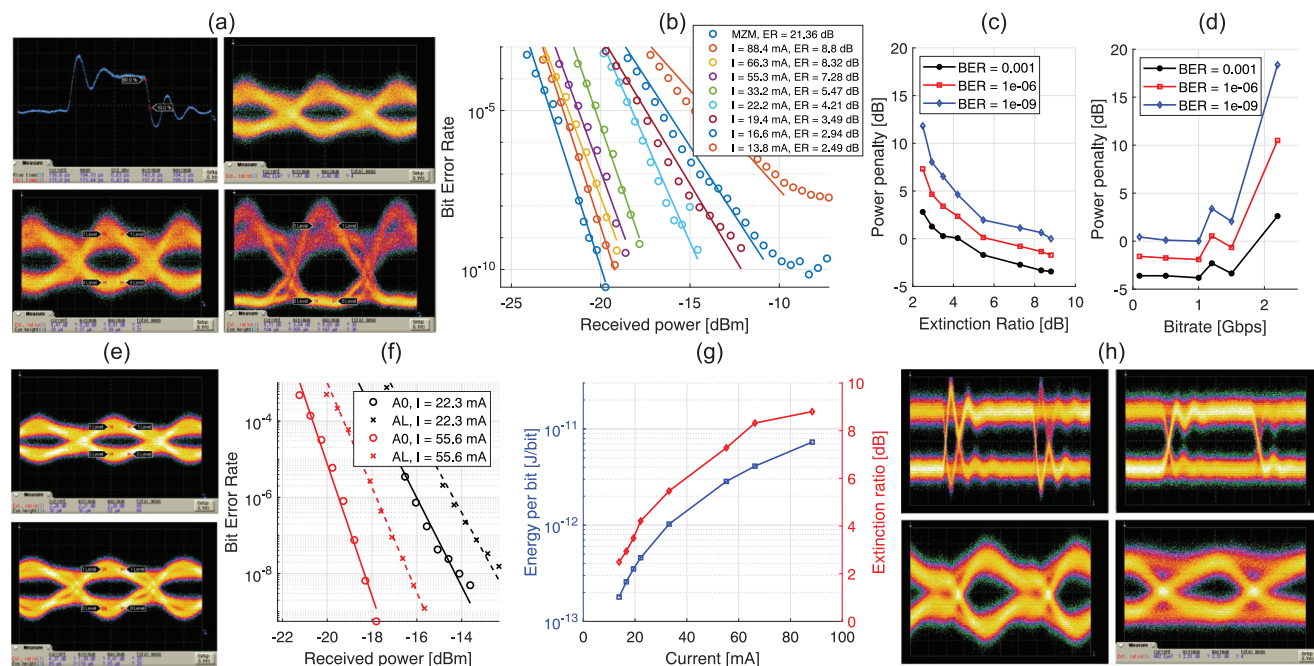


Figure 6. a) Waveform demonstrating the rising and falling edge times and three eye diagrams at 13.8, 33.2, and 88.4 mA (top right, bottom left, and bottom right, respectively). b) bit error rate (BER) curves versus the received input power of a reference Mach-Zehnder modulator (MZM) and the MRR at various current levels and a PRBS-31 sequence. c) Power penalty for various ER at three BERs. d) Power penalty for various bitrates at 33.2 mA for three BERs. A PRBS-7 sequence is used. e) Eye diagrams where the laser is aligned to the linear section of the notch at 22.2 and 55.3 mA (top and bottom, respectively). f) BER performance difference with a linear aligned eye (AL, dashed lines) and where the zero-level is aligned to the center of the notch (A0, solid lines). g) Extinction ratio versus current and the energy consumption per bit versus current. h) Eye diagrams of using an AWG to limit the bandwidth of the input signal. The top and bottom rows show 200 Mbps and 1 Gbps, respectively.

Ltd., max. 10 Gbps, zero chirp MZM) is used as a reference. For the modulator, the laser is aligned such that the zero level is located in the minimum of the notch. The results in Figure 6a,b shows that the modulator performance improves with increasing modulating current. All points have been fitted with linear curves. Above 20 mA, the fitting error is small and all curves demonstrate error-free operation (i.e., BER 10^{-9}). An error floor appears below 20 mA. At 13.8 mA, error-free operation is not possible. Especially at low currents, where the ER is low, the results are sensitive to noise and the fibre alignment of the setup. The power penalty versus the ER is demonstrated in Figure 6c. With the received optical power referenced at 88.4 mA for a BER of 10^{-9} , 16.6 mA (ER of 2.94 dB) gives a power penalty of 8.0 dB.

Next, Figure 6d shows the impact of bitrate on the power penalty. The graph shows that the transient limits the performance to around 1.5 Gbps. At higher bitrates, the BER performance degrades quickly. For example, at 2 Gbps, no error-free transmission is possible, where at 2.2 Gbps, the transient allows for a very small eye.

The alignment sensitivity of the modulator in terms of wavelength is demonstrated in Figure 6e,f. The solid lines represent a laser alignment with the zero-level in the notch of the modulator spectrum (A0, top eye), the dashed lines represent a alignment in the linear region of the notch (AL, bottom eye). For both current levels, the power penalty is about 1.5 dB. The A0 alignment gives a clear advantage when linearity is not needed.

Figure 6g shows the trade-off between power consumption and ER. By increasing the current, the opening of the eye and the ER

increases. The exponential shape is similar to Figures 3c and 4d. Further increasing the ER comes at a cost of a significant increase in power consumption. This behavior is similar to the model, where the RWS is large causing the ER to saturate. The values for E_b are calculated using Equation (6), with $R = 1 \Omega$ and $L = 200 \text{ pH}$ (characterized by Pintus et al.,^[9]). For efficient operation, 16.6 mA of current results in error-free transmission for only 258 fJ bit⁻¹.

At 1.2 Gbps, the eye diagram is open. Using a different bitrate, the transient can severely distort the waveform. Using an arbitrary waveform generator (AWG), the rise time of the RF feed signal has been reduced to minimize the transient. Figure 6h shows the effect at 200 Mbps (top) and 1 Gbps (bottom). Ideally, the signal should be generated using the inverse modulator response, but a faster AWG was not available at the time.

6. Discussion

By modeling and characterizing a MO modulator, we have built a large set of tools to achieve greater insight in magneto-optics. The model shows confident steady-state results, calculates the MO effect accurately and gives insights in the dynamic response of the optical device. The characterization has confirmed the MRR model and shows us that MO based modulation works.

Efficiency is an important driver for MO based modulators. The model demonstrates that the achieved fJ bit⁻¹ efficiency could be further improved by tweaking the design of the MRR. By tuning the resonator gap, the critical coupling point can be shifted. This reduces the energy required to shift the spectrum and leads

Table 1. Comparison of the MO modulator to similar state-of-the-art modulators.

Platform	Structure	Year	BW [GHz]	IL [dB]	Pk. ER [dB]	R [Gbps]	Footprint [μm^2]	E_b [fJ bit $^{-1}$]	Source
ITO on SOI	PC	2020	1.9	7.8	3.5	3	43	18.3	[5]
SOI	MRR	2015	-	1.8	6.2	6	1500	5	[4]
SOI	MRR	2009	11	2	15	10	1000	50	[40]
SOI	MRR	2012	1.7	3	8	2	100	180	[41]
SOI + Ce:YIG	MRR	2022	5.5	25	2.9	1.2	1600	258	This work

BW, Bandwidth; IL, insertion loss; ER, extinction ratio; R, data rate; ITO, indium tin oxide; SOI, silicon on insulator; PC, photonic crystal; MRR, microring resonator.

to a stronger optical isolation. The cost of a larger gap is a higher Q -factor, reduced modulation speed, and spectral bandwidth. The latter causing laser tuning and stabilization to become more critical. Using different MO materials or improving magnetic coupling helps to improve the efficiency, but Figure 3g proves that the actual improvement in terms of ER versus current is limited, especially when low Q resonators are desired.

Electrically, the efficiency could be further improved from 258 fJ bit $^{-1}$ to tens of fJ bit $^{-1}$ by ironing the transient out to achieve higher bitrates. The driver is not considered in this estimation. Note that no commercial drivers exist that are able to efficiently power the modulator. Novel designs are needed to handle the inductance of the coils at high bitrates, whilst maintaining maximum efficiency (i.e., beyond 80%). Impedance matching could help to improve efficiency even further, by minimizing the reflected—and hence wasted—power. Adhering to the 50 Ω standard might be beneficial for compatibility, but opting for lower matched impedances will help to keep added resistive losses to a minimum.

At last, Ce:YIG has demonstrated to be sufficiently powerful to modulate light. Even though the model has demonstrated a low impact of the MO effect on the modulating efficiency, material engineering on Ce:YIG would be useful to reduce overall optical losses. Given that the characterized device showed a weaker MO effect (Figure 3f), it might be viable to opt for different materials with a weaker MO effect. This might be favorable when the replacing MO materials are more transparent and easier to fabricate and deposit on platforms such as SOI, SiN, or InP.

Compared to various mature EO modulators from Table 1, competing state-of-the-art, low-speed, and small modulators do not significantly outperform the characterized MO modulator at 16.6 mA. It seems that with some optimization MO modulators can become a great power-efficient tool. Ideally, the propagation losses and the efficiency of the MO effect should be improved, as demonstrated in the model, such that operation with single or sub-mA currents are possible. Regardless, the results are surprisingly promising and give confidence for future versions.

7. Conclusion

A magneto-optic modulator has been modeled electrically and optically to assess its dynamic performance and energy efficiency. Results show efficient operation of 155 fJ bit $^{-1}$ at 1.2 Gbps with an extinction ratio of 24.6 dB. Characterization of a similar device demonstrates error-free operation at 16.6 mA with an extinction ratio of 2.9 dB. Extinction ratios up to 8.8 dB can be achieved

using a higher drive current. Our investigation shows that the magneto-optic effect has large potential to enable energy efficient data transmission links.

Acknowledgements

P.P., D.H., and J.E.B. would like to thank the Air Force Office of Scientific Research (award number FA9550-21-1-0042). Any opinions, findings, and conclusions or recommendations expressed in this material are those of the authors and do not necessarily reflect the views of the United States Air Force.

Conflict of Interest

The authors declare no conflict of interest.

Data Availability Statement

The data that support the findings of this study are available from the corresponding author upon reasonable request.

Keywords

cerium substituted yttrium iron garnet, magneto-optics, micro-ring resonators, modulators, silicon photonics

Received: October 21, 2022

Revised: December 22, 2022

Published online:

- [1] D. A. B. Miller, in *Proc. of 2021 Optical Fiber Communications Conf. and Exhibition (OFC)*, IEEE, Piscataway, NJ **2021**, pp. 1–2.
- [2] C. A. Thraskias, E. N. Lallas, N. Neumann, L. Schares, B. J. Offrein, R. Henker, D. Plettemeier, F. Ellinger, J. Leuthold, I. Tomkos, *IEEE Commun. Surv. Tutorials* **2018**, *20*, 2758.
- [3] P. Srinivasan, K. Muth, K. Masuda, M. Alalusi, S. Steinbach, M. Ziebell, A. Trita, H. Yang, F. Peters, A. Zilkie, in *Proc. of 45th European Conf. on Optical Communication (ECOC 2019)*, IEEE, Piscataway, NJ **2019**, pp. 1–3.
- [4] K. T. Settaluri, S. Lin, S. Moazeni, E. Timurdogan, C. Sun, M. Moresco, Z. Su, Y. H. Chen, G. Leake, D. Latulipe, C. McDonough, J. Hebding, D. Coolbaugh, M. Watts, V. Stojanović, in *Proc. of ESSCIRC Conf. 2015-41st European Solid-State Circuits Conf. (ESSCIRC)*, IEEE, Piscataway, NJ **2015**, pp. 156–159.
- [5] E. Li, B. Zhou, Y. Bo, A. X. Wang, *arXiv:2004.00983*, **2020**.

- [6] S. Wolf, H. Zwickel, W. Hartmann, M. Laueremann, Y. Kutuvantavida, C. Kieninger, L. Altenhain, R. Schmid, J. Luo, A. K. Jen, S. Randel, W. Freude, C. Koos, *Sci. Rep.* **2018**, *8*, 2598.
- [7] R. Sobolewski, J. R. Park, *IEEE Trans. Appl. Supercond.* **2001**, *11*, 727.
- [8] S. E. Irvine, A. Y. Elezzabi, *Proc. SPIE* **2003**, 5260, 580.
- [9] P. Pintus, L. Ranzani, S. Pinna, D. Huang, M. V. Gustafsson, F. Karinou, G. A. Casula, Y. Shoji, Y. Takamura, T. Mizumoto, M. Soltani, J. E. Bowers, *Nat. Electron.* **2022**, *5*, 604.
- [10] R. Yasuhara, S. Tokita, J. Kawanaka, T. Kawashima, H. Kan, H. Yagi, H. Nozawa, T. Yanagitani, Y. Fujimoto, H. Yoshida, M. Nakatsuka, *Opt. Express* **2007**, *15*, 11255.
- [11] R. Verreault, *Solid State Commun.* **1969**, *7*, 1653.
- [12] O. Slezák, R. Yasuhara, A. Lucianetti, T. Mocek, *Opt. Mater. Express* **2016**, *6*, 3683.
- [13] X. Xue, B. Patra, J. P. G. van Dijk, N. Samkharadze, S. Subramanian, A. Corna, B. Paquetel Wuetz, C. Jeon, F. Sheikh, E. Juarez-Hernandez, B. P. Esparza, H. Rampurawala, B. Carlton, S. Ravikumar, C. Nieva, S. Kim, H.-J. Lee, A. Sammak, G. Scappucci, M. Veldhorst, F. Sebastiano, M. Babaie, S. Pellerano, E. Charbon, L. M. K. Vandersypen, *Nature* **2021**, 593, 205.
- [14] D. J. Reilly, *arXiv:1912.05114*, **2019**.
- [15] A. Ganguly, S. Abadal, I. Thakkar, N. E. Jerger, M. Riedel, M. Babaie, R. Balasubramonian, A. Sebastian, S. Pasricha, B. Taskin, *IEEE Micro* **2022**, *42*, 40.
- [16] D. Huang, P. Pintus, C. Zhang, Y. Shoji, T. Mizumoto, J. E. Bowers, *IEEE J. Sel. Top. Quantum Electron.* **2016**, *22*, 271.
- [17] D. Huang, P. Pintus, Y. Shoji, P. Morton, T. Mizumoto, J. E. Bowers, *Opt. Lett.* **2017**, *42*, 4901.
- [18] D. Huang, P. Pintus, J. Peters, P. A. Morton, Y. Shoji, T. Mizumoto, J. E. Bowers, in *Proc. of IEEE 15th Int. Conf. Group IV Photonics, GFP, IEEE, Piscataway, NJ* **2018**, pp. 1–2.
- [19] D. Huang, P. Pintus, C. Zhang, P. Morton, Y. Shoji, T. Mizumoto, J. E. Bowers, *Optica* **2017**, *4*, 23.
- [20] P. Pintus, D. Huang, P. A. Morton, Y. Shoji, T. Mizumoto, J. E. Bowers, *J. Lightwave Technol.* **2019**, *37*, 1463.
- [21] C. J. Firby, P. Chang, A. S. Helmy, A. Y. Elezzabi, *JOSA B* **2018**, *35*, 1504.
- [22] L. Li, X. Zong, Y. Liu, *J. Phys. D: Appl. Phys.* **2020**, *53*, 185106.
- [23] C. J. Firby, A. Y. Elezzabi, *Optica* **2015**, *2*, 598.
- [24] R. M. Crutcher, A. J. Kemball, *Front. Astron. Space Sci.*, <https://doi.org/10.3389/fspas.2019.00066>.
- [25] A. K. Zvezdin, V. A. Kotov, *Modern Magneto-optics and Magneto-optical Materials*, CRC Press, Boca Raton, FL **1997**.
- [26] D. Jalas, *Ph.D. Thesis*, Technischen Universität Hamburg, Hamburg **2018**.
- [27] Y. Yazaki, Y. Shoji, T. Mizumoto, *Jpn. J. Appl. Phys.* **2007**, *46*, 5460.
- [28] M. C. Onbasli, L. Beran, M. Zahradník, M. Kucera, R. Antoš, J. Mistrík, G. F. Dionne, M. Veis, C. A. Ross, *Sci. Rep.* **2016**, *6*, 23640.
- [29] Y. Zhang, Q. Du, C. Wang, T. Fakhru, S. Liu, L. Deng, D. Huang, P. Pintus, J. Bowers, C. A. Ross, J. Hu, L. Bi, *Optica* **2019**, *6*, 473.
- [30] T. Fakhru, S. Tazlaru, L. Beran, Y. Zhang, M. Veis, C. A. Ross, *Adv. Opt. Mater.* **2019**, *7*, 1900056.
- [31] A. Lopez-Santiago, H. R. Grant, P. Gangopadhyay, R. Voorakaranam, R. A. Norwood, N. Peyghambarian, *Opt. Mater. Express* **2012**, *2*, 978.
- [32] W. Bogaerts, P. de Heyn, T. van Vaerenbergh, K. de Vos, S. K. Selvaraja, T. Claes, P. Dumon, P. Bienstman, D. van Thourhout, R. Baets, *Laser Photonics Rev.* **2012**, *6*, 47.
- [33] P. Pintus, *Opt. Express* **2014**, *22*, 15737.
- [34] P. Pintus, D. Huang, C. Zhang, Y. Shoji, T. Mizumoto, J. E. Bowers, *J. Lightwave Technol.* **2017**, *35*, 1429.
- [35] Q. Xu, B. Schmidt, J. Shakya, M. Lipson, *Opt. Express* **2006**, *14*, 9431.
- [36] J. M. D. Coey, *Magnetism and Magnetic Materials*, Cambridge University Press, Cambridge **2001**.
- [37] W. R. McKinnon, D.-X. Xu, C. Storey, E. Post, A. Densmore, A. Delâge, P. Waldron, J. H. Schmid, S. Janz, *Opt. Express* **2009**, *17*, 18971.
- [38] R. Zhang, Y. He, Y. Zhang, S. An, Q. Zhu, X. Li, Y. Su, *Nanophotonics* **2020**, *10*, 937.
- [39] P. Pintus, M. Hofbauer, C. L. Manganelli, M. Fournier, S. Gundavarapu, O. Lemonnier, F. Gambini, L. Adelmini, C. Meinhardt, C. Kopp, F. Testa, H. Zimmermann, C. J. Oton, *Laser Photonics Rev.* **2019**, *13*, 1800275.
- [40] P. Dong, S. Liao, D. Feng, H. Liang, D. Zheng, *Opt. Express* **2009**, *17*, 22484.
- [41] J. V. Campenhout, M. Pantouvaki, P. Verheyen, S. Selvaraja, G. Lepage, H. Yu, W. Lee, J. Wouters, D. Goossens, M. Moelants, W. Bogaerts, P. Absil, in *Optical Fiber Communication Conference*, Optical Society of America, Washington, D.C **2012**, OM2E.4.